

Modelling the very large-scale connectome

Géza Ódor (1), Michael Gastner (2), Jeffrey Kelling (3),
Gustavo Deco (4)

(1) Institute of Technical Physics and Materials Science, Center for Energy Research,
P. O. Box 49, H-1525 Budapest, Hungary

(2) Yale-NUS College, Division of Science, 16 College Avenue West, #01-220
Singapore 138527

(3) Department of Information Services and Computing, Helmholtz-Zentrum Dresden
- Rossendorf, P.O.Box 51 01 19, 01314 Dresden, Germany

(4) Center for Brain and Cognition, Theoretical and Computational Group,
Universitat Pompeu Fabra / ICREA, Barcelona, Spain

E-mail: odor@mfa.kfki.hu

April 2021

Abstract. In this review, we discuss critical dynamics of simple nonequilibrium models on large connectomes, obtained by diffusion MRI, representing the white matter of the human brain. In the first chapter, we overview graph theoretical and topological analysis of these networks, pointing out that universality allows selecting a representative network, the *KKI-18*, which has been used for dynamical simulation. The critical and sub-critical behaviour of simple, two- or three-state threshold models is discussed with special emphasis on rare-region effects leading to robust Griffiths Phases (GP). Numerical results of synchronization phenomena, studied by the Kuramoto model, are also shown, leading to a continuous analog of the GP, termed frustrated synchronization in Chimera states. The models presented here exhibit avalanche scaling behaviour with exponents in agreement with brain experimental data if local homeostasis is provided.

1. Introduction

The organization of resting-state activity (i.e. the dynamics of the brain in the absence of external stimulation and without task condition) presumably plays a critical functional role because maintenance requires a large part of the total energy budget of the brain [1, 2]. There is empirical and computational evidence showing that the resting organization facilitates task-based information processing [3]. Resting brain networks, as captured by functional connectivity maps, consistently show that individual differences in functional connectivity can predict individual differences in task-evoked regional activity [4–6]. From a mechanistic perspective, whole-brain models can demonstrate that resting-state organization conforms to a state of criticality

that promotes responsiveness to external stimulation (i.e. resting-state organization facilitates task-based processing) [7–9].

Neuronal avalanches are cascading sequences of increasing activations that reveal critical behaviour, in which brain functions are optimized by enhancing, for example, input sensitivity and dynamic range [10]. This criticality-based optimization is sustained, thanks to the underlying particular operating regime perched at the brink between phases of order and disorder. Criticality is explicitly reflected by the scaling invariance of the sizes and durations of neuronal avalanches. A signature of criticality is given by the fact that the sizes and durations of neuronal avalanches follow power-law statistics with exponents that depend on each other. Furthermore, Friedman et al. [11] demonstrated another signature of criticality, namely scaling similarity, by showing that the dynamics of long-duration avalanches are similar to those of short-duration avalanches when they are properly rescaled.

The criticality hypothesis has been proposed because information processing, sensitivity, long-range and memory capacity is optimal in the neighbourhood of criticality [12–15]. Criticality in statistical physics is defined by diverging correlation lengths and times as we tune a control parameter to a threshold value. As a consequence, microscopic details are irrelevant, and universal critical scaling exponents appear in general.

During the last decade, criticality was shown in neuronal recordings (spiking activity and local field potentials, LFPs) of neural cultures *in vitro* [11, 16–18], LFP signals *in vivo* [19], field potentials and functional magnetic resonance imaging (fMRI) blood-oxygen-level-dependent (BOLD) signals *in vivo* [20, 21], voltage imaging *in vivo* [22], and 10–100 single-unit or multi-unit spiking and calcium-imaging activity *in vivo* [23–26]. Furthermore, source reconstructed magneto- and electroencephalographic recordings (MEG and EEG), characterizing the dynamics of ongoing cortical activity, have also shown robust power-law scaling in neuronal long-range temporal correlations (LRTC). These are at time scales from seconds to hundreds of seconds and describe behavioural scaling laws consistent with concurrent neuronal avalanches [27]. However, the measured scaling exponents do not seem to be universal. Instead, they are scattered around the mean-field values of the directed percolation universality class [28]. It is worth mentioning that LRTC allow investigating scaling at different time scales than avalanche measurements, which span only in the 0.001–0.1 s range. Similarly, recent calcium imaging recordings of dissociated neuronal cultures show that the exponents are not universal, and significantly different exponents arise with different culture preparations [29]. Thus, the single mean-field universality class hypothesis has been challenged. This diversity has also been studied by experiments and simulations. Quasicriticality, generated by external excitations, was suggested to explain the lack of universality observed in different experiments [30].

Nevertheless, at the whole-brain level, criticality remains still an open question. Mesoscopic local measurements (e.g. LFP or spiking activity) might introduce a bias due to the limited number of neurons and, consequently, are sensitive to subsampling

effects [23, 31, 32]. Furthermore, in electrode experiments, there is uncertainty about partitioning and binning of activity spots into avalanches. Earlier, temporal closeness of measured spikes was used to determine the beginning and the end of activity spikes [33], but later this method was criticized [34], and data analysis has become more careful. On the other hand, BOLD or MEG signals might not capture the global dynamics if the parcellation used is too coarse. Therefore, to study criticality in the nervous system, it is necessary to monitor whole-brain dynamics with high resolution.

Until now, structural network studies were performed on much smaller-sized connectomes. For example, the data obtained by Sporns and collaborators, using diffusion imaging techniques [35, 36], consist of a highly coarse-grained mapping of anatomical connections in the human brain, comprising $N = 998$ brain areas and the fiber tract densities between them. In order to prove real power laws, valid for several decades, one needs to consider larger-sized systems, lack of corrections to scaling and size cutoff [37]. Therefore, we have downloaded the largest available human connectomes and run numerical simulations to test the criticality hypothesis, with a focus on heterogeneity effects and the possibility of emergence of dynamical criticality sub-critically. Since this graph has a topological dimension $d < 4$ [38], a real synchronization phase transition is not possible in the thermodynamic limit. Still, we could locate a transition between partially synchronized and de-synchronized states. In this review, we show simulation results based on direct measurements of characteristic times and sizes instead of using avalanche spot binning.

It has been debated how a neural system is tuned to criticality. At first, self-regulatory mechanisms [39], leading to self-organized criticality [40], were proposed. Let us remark that, as a consequence of heterogeneity, extended dynamical critical regions with non-universal scaling emerge naturally in spreading models [37, 41]. If quenched heterogeneity (i.e. disorder with respect to a homogeneous system) is present, rare-region effects [42] and an extended *semi-critical* region where spatial correlations do not diverge, known as Griffiths Phase (GP) [43], can emerge. Rare regions are very slowly relaxing domains that remain, for a long time, in the phase that is the opposite of the phase of the whole system, causing slow evolution of the order parameter. In the entire GP, which is an extended control parameter region around the critical point, the susceptibility diverges, providing a high sensitivity to stimuli, which is beneficial for information processing. Auto-correlations follow fat-tailed power-laws, resulting in burstiness [44], which is a frequently observed phenomenon in human behaviour [45]. Even in infinite-dimensional systems, where mean-field behaviour is expected, Griffiths effects [46] may occur in finite time windows. As real systems are mostly inhomogeneous, one must assess whether the heterogeneity is weak enough to justify the usage of homogeneous models for describing them. It was also proposed that a GP might be the reason for the working memory in the brain [47].

As individual neurons emit periodic signals [48], it is natural to expect criticality in oscillator models at the synchronization transition point. Recently, an analysis of Ginzburg–Landau-type equations concluded that empirically reported scale-invariant

avalanches can possibly arise if the cortex is operated at the edge of a synchronization phase transition, where neuronal avalanches and incipient oscillations coexist [49]. Several oscillator models have been used in biology. The simplest one is the Hopf model [50], which has been used frequently in neuroscience because it can describe a critical point with scale-free avalanches that have a sharpened frequency response and enhanced input sensitivity.

Another complex model, describing more non-linearity, is the Kuramoto model [51, 52] that was studied analytically and computationally in the absence of frequency heterogeneity on a human connectome graph with 998 nodes and on hierarchical modular networks, in which moduli exist within moduli in a nested way at various scales [53]. Because of quenched, purely topological heterogeneity, an intermediate phase was found between the standard synchronous and asynchronous phases, showing “frustrated synchronization”, meta-stability and chimera-like states [54]. This complex phase was investigated further in the presence of noise [55] and on a simplicial complex model of manifolds with finite and tunable spectral dimension [56] as a simple model for the brain.

The dynamical behaviour of the heterogeneous Kuramoto model, especially for local interactions, is a largely unexplored field to the best of our knowledge. In case of identical oscillators, heterogeneous phase lags or couplings have been shown to result in partial synchronization and stable chimera states [57–60]. Realistic models of the brain, however, require oscillators [61] to be heterogeneous. Consequently, the main focus of this review is to discuss criticality at the whole-brain level from the perspective of synchronization in the heterogeneous Kuramoto model.

2. Human connectome topology

The connectome is defined as the structural network of neural connections in the brain [62]. The human brain has $\approx 10^{11}$ neurons, which current imaging techniques cannot comprehensively resolve at the scale of single neurons. Studies must, therefore, work with coarse-grained data. Early studies, based on 998 large-scale cortical regions, gave some insights into the relation between structural and functional connectivity [35, 36]. They found that, although strong functional connections exist between regions that have no direct structural connection, resting state functional connectivity is constrained by the connectome structure. Here, we review results about the human connectome at a more fine-grained level ($\approx 10^6$ nodes). The results are based on diffusion tensor imaging data by Landman et al. [63]. Diffusion tensor imaging has generally been found to be in good agreement with ground-truth data from histological tract tracing [64]. Inferred networks of structural connections were made available by the Open Connectome Project and previously analyzed by Gastner and Ódor [38]. These graphs are symmetric, weighted networks, where the weights measure the number of fiber tracts between nodes.

2.1. Degree distribution

Since the early days of complex network science, it has often been hypothesized that structural and functional brain networks have power-law degree distributions [65–67]. In statistical physics, power laws occur at transitions between ordered and disordered phases. Because circumstantial evidence supported the hypothesis that the brain operates near such a critical point [33, 68, 69], a power-law degree distribution appeared to be a plausible assumption. However, observational data of structural brain networks did not support the power-law hypothesis [70–72].

In [38], we applied model selection based on the Akaike information criterion to determine which probability distributions fit the Open Connectome data best. The investigated candidate distributions for model selection were power-law, exponential, log-normal and Weibull distributions. In the case of the power-law and Weibull distributions, we also considered three-parameter generalizations: a truncated power law, $P(\text{degree} \geq k) \propto \alpha^\beta (k + \alpha)^{-\beta} e^{-\gamma k}$, and a generalized Weibull distribution [73], $P(\text{degree} \geq k) \propto \exp[\alpha(\gamma^\beta - (k + \gamma)^\beta)]$, where k is the degree, and α , β and γ are parameters to be fitted to data. We also allowed each candidate model to be valid only for sufficiently large degree k because corrections may, in practice, need to be applied to small degrees. The Akaike information criterion imposes a penalty for every additional parameter in the model that must be fitted to data. We applied the criterion by Burnham and Anderson [74] that there is only empirical support for a statistical model if the corresponding Akaike information criterion differs by less than 10 from the minimum for all candidate models.

We fitted parameters to ten human connectomes and found that, in nine cases, there was at least some empirical support for a generalized Weibull distribution. In seven cases, there was a similar level of evidence for a truncated power law. There was little or no empirical support for any other candidate model, which excludes power law tails from the set of plausible assumptions. Given empirical brain data, the Akaike information criterion generally favored models with a larger number of parameters, which implies that it is difficult to mimic the true complexity of the connectome topology with simple models. Therefore, we recommend that simulations of brain dynamics are performed on empirical, rather than modeled, networks if possible.

2.2. Small-world topology

Apart from the degree distribution, dynamic processes on networks also depend on the paths between nodes. A common feature of many real-world complex networks is their small-world topology [75]. A network is called a small world if there is, on one hand, a tendency for nodes to form local clusters, but, on the other hand, there are also long-distance links that significantly reduce the average of the shortest path lengths L between all pairs of nodes. The inter-areal network of large-scale brain regions is a small world [76], but it remains an open question whether the connectome is also a small-world network at a cellular level [77].

To shed light on this issue, we quantified the small-world coefficient σ , defined in [78], for Open Connectome networks [38]. The small-world coefficient compares the clustering coefficient C and the average path length L with the corresponding values C_r and L_r of an Erdős–Rényi random graph according to the formula

$$\sigma = \frac{C/C_r}{L/L_r}. \quad (1)$$

By definition, a small-world network satisfies $\sigma > 1$. For the Open Connectome data, we found that σ is in the range from 750 to 890 if the clustering coefficient is measured with the Watts-Strogatz formula [75]. We found no significant dependence of σ on the number of nodes. Thus, connectomes are small-world networks, and σ can be treated as scale-independent.

2.3. Topological dimension

The small-world coefficient σ captures the relation between local clustering and the mean topological distance (i.e. the average of the minimum number of edges on a path between two nodes). Another measure of interest is the topological dimension D , which characterizes how quickly neighbourhoods increase as a function of distance. If N_r is the number of node pairs within a distance $\leq r$, then the topological dimension D is the exponent that fits best to the relation $N_r \propto r^D$. It has been conjectured that a finite dimension D is indicative of Griffiths phases and rare-region effects, which might explain power-laws and scale invariance observed in brain network dynamics [79].

From the Open Connectome data, power-law fits in the range $1 \leq r \leq 5$ (Fig. 1) suggest topological dimensions between $D = 3$ and $D = 4$ [38]. For larger r , N_r saturates because the number of nodes in the network is finite, so the range over which $\log(N_r)$ increases linearly in $\log(r)$ is small. In the inset of Fig. 1, we plot the discretized derivative

$$D_{\text{eff}}(r + 1/2) = \frac{\ln N_r - \ln N_{r+1}}{\ln(r) - \ln(r + 1)}. \quad (2)$$

We estimated D in the limit of large network size by extrapolating D_{eff} (dashed lines in Fig. 1). We detected a tendency that larger networks have larger values of D . However, the increase is small so that Griffith phases in brain dynamics are plausible.

2.4. Universality and homeostasis

The network topology study exhibits a certain level of universality in the topological features of the human connectomes: degree distributions, graph dimensions, clustering and small world coefficients. One may expect the same dynamical behaviour to occur in dynamical simulation on human connectome graphs. Therefore, one of the graphs, called *KKI-18*, was selected to be the representative in further studies. The graph, downloaded in 2015 from the Open Connectome project repository [80], was generated via the MIGRAINE method [81]. It comprises a large component with $N = 804\,092$

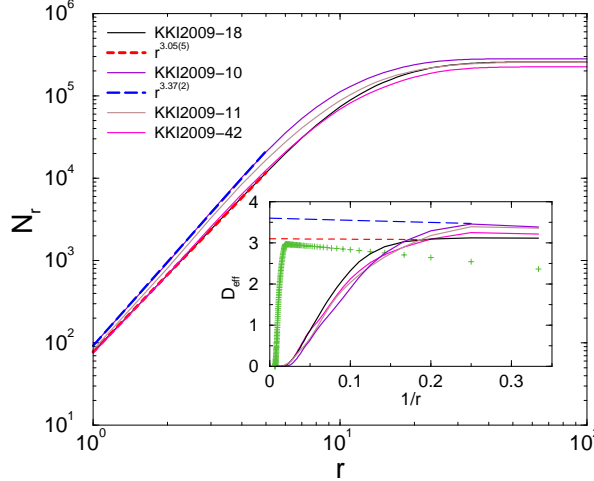


Figure 1. Number of nodes within graph distance r in four different KKI connectomes. Dashed lines show power-law fits. Inset: local slopes defined in Eq. 2. Crosses correspond to measurements on a regular 100^3 lattice. Figure from [38].

nodes connected via 41 523 908 undirected edges and several small disconnected sub-components, which were ignored in the modelling.

KKI-18 exhibits hierarchical modular structure because it is constructed from cerebral regions in the Desikan Atlas [?] with (at least) two different scales. The graph topology is shown in Fig. 2, in which modules were identified by the Leiden algorithm [82]. It found 153 modules, with sizes varying between 7 and 35 332 nodes.

Weights between nodes i and j of this graph vary between 1 and 854. The probability density function is shown in Fig. 2. Following a sharp drop, one can observe a power-law region for $20 < w_{ij} < 200$ with cutoff at large weights. The average weight of the links is $\simeq 5$. Note that the average degree of this graph is $\langle k \rangle = 156$ [38], whereas the average number of the incoming weights of nodes is $\langle W_i \rangle = 1/N \sum_i \sum_j w_{ij} = 448$.

In Refs. [83, 84], it was shown that dynamical models running on the KKI-18 graph do not exhibit a critical transition. Due to the large weight differences and graph dimensionality, the hubs cause catastrophic, discontinuous transitions.

Homeostasis in real brains occurs via inhibitory neurons [8, 85–88]. In our studies, we modeled this effect by normalizing the incoming interaction strengths [83]. To keep the local sustained activity requirement for the brain [89] and to avoid nodes which practically cannot affect the activity propagation, the incoming weights were renormalized by their sum

$$W'_{ij} = W_{ij} / \sum_{j \in \text{neighb. of } i} W_{ij} . \quad (3)$$

The renormalization makes the system homeostatic, and simulations showed the occurrence of criticality as well as Griffiths effects. Indeed, there is some evidence that neurons have a certain adaptation to their input excitation levels [90] and can be modeled by variable thresholds [91]. Recent theoretical studies have also suggested that

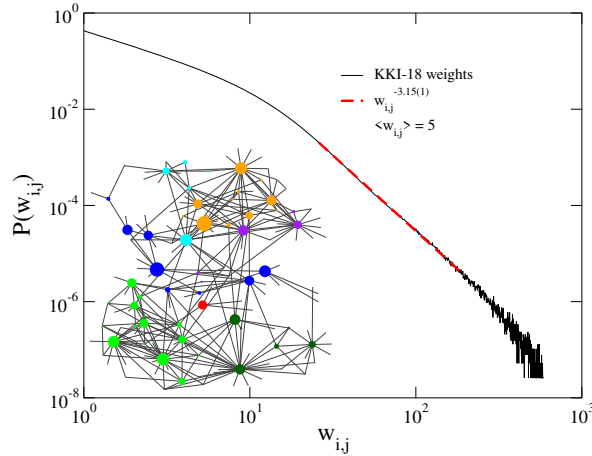


Figure 2. Probability distribution function of link weights in the *KKI-18* connectome. Dashed line: a power-law fit for intermediate weights. Inset: network of the modules of the *KKI-18* human connectome graph obtained through Leiden community analysis. The areas of the circles is proportional to the number of nodes. Each circle's color indicates its membership in one of seven modules of the displayed graph of modules, illustrating the hierarchical nature of *KKI-18*.

homeostatic plasticity mechanisms may play a role in facilitating criticality [8, 86–88]. Recently, a comparison of modelling and experiments arrived at a similar conclusion: equalized network sensitivity improves the predictive power of a model at criticality in agreement with the fMRI correlations [92].

3. Critical dynamics of discrete threshold models on the Connectome

To understand the collective behaviour of a large amount of neurons, simple discrete models have been used in computer simulations [89, 93]. The *KKI-18* connectome was first studied using a two-state threshold model in which sites could be inactive or active: $x_i = 0$ or 1 [83]. Later, this study was extended to a three-state model [94] in which sites could become refractory ($x_i = -1$) for one time step, when the activity of the state was lost, before becoming inactive. This prevents activated neighbours from immediately reactivating the source, which can lead to propagating fronts, resembling dynamical percolation [95]. However, this critical behaviour could occur only in the infinitely long refractory state limit. The application of refractory states is a common feature in brain modelling [96].

Dynamical processes, mimicking neuronal avalanches, were initiated by activating a randomly selected 'seed' node. At each network update, every node (i) was visited and tested if the sum of incoming weights W_{ij} of active neighbours reached a given threshold

value

$$\sum_j \delta(x_j, 1) W_{ij} > K , \quad (4)$$

where $\delta(i, j)$ is the Kronecker delta function. If this condition was met, activation of $x_i = 0$ was attempted with probability λ . Alternatively, an active node was deactivated with probability ν . For the refractory version, the intermediate state ($x_i = 1 \rightarrow x_i = -1$) was set with probability 1 and deactivation to $x_i = 0$ was done only at the following graph update.

New states of the nodes were overwritten only after a full network update. Until then, they were stored in a temporary state vector. This procedure means that synchronous updates were performed at discrete time steps. The updating process continued as long as active sites were available or up to a maximum time limit of $t = 10^6$ to 10^7 Monte Carlo sweeps. For this stochastic cellular automaton, synchronous updating is not expected to affect the dynamical scaling behaviour [41] because there are no activity currents. Synchronous updating makes it possible to implement parallel algorithms. In fact, the code was implemented on GPUs, which resulted in a $12\times$ speedup with respect to contemporary CPU cores.

In case the system had fallen into the inactive state, the actual time step was recorded in order to calculate the survival probability $p(t)$ of runs. The average activity

$$\rho(t) = 1/N \sum_{i=1}^N \delta(x_i, 1) \quad (5)$$

and the total number of activated nodes

$$s = \sum_{i=1}^N \sum_{t=1}^T \delta(x_i, 1) \quad (6)$$

during the avalanche of duration T was calculated at the end of the simulations.

By varying the control parameters (K , λ and ν), one can locate the transition point between active and absorbing steady states. At critical phase transition points, the avalanche survival probability is expected to scale asymptotically as

$$P(t) \propto t^{-\delta} , \quad (7)$$

where δ is the survival probability exponent [97]. This scaling law is connected to the avalanche-duration scaling

$$p(t) \propto t^{-\tau_t} . \quad (8)$$

Integration in time imposes the exponent relation

$$\tau_t = 1 + \delta. \quad (9)$$

In seed simulations, the number of active sites initially grows as

$$N(t) \propto t^\eta , \quad (10)$$

with the exponent η , related to the avalanche size distribution

$$p(s) \propto s^{-\tau} , \quad (11)$$

via the exponent relation [98]

$$\tau = (1 + \eta + 2\delta)/(1 + \eta + \delta) . \quad (12)$$

To analyze corrections to scaling, one can calculate the local slopes of the dynamical exponents δ and η as the discretized, logarithmic derivatives of (7) and (10). For example, the effective exponent of δ is measured as

$$\delta_{\text{eff}}(t) = -\frac{\ln P(t) - \ln P(t')}{\ln(t) - \ln(t')} , \quad (13)$$

using $t - t' = 8$ or 4 . These difference selections have been found to be optimal in noise reduction versus effective exponent range [95]. Similarly, one can also define $\eta_{\text{eff}}(t)$.

In Ref. [83], results were obtained for two-state threshold models on directed, randomly diluted edge variants of the KKI-18 network. The results were compared with those of the original, undirected graph and showed qualitative invariance of the GP for those changes. Figure 3 shows the activity avalanche survival probability $p(t)$ for the threshold $K = 0.25$ and deactivation probability $\nu = 0.9, 0.95$ on the *KKI-18* connectome. One can see power-law tails for more than three decades with continuously changing exponents as we vary λ and ν .

The critical point, above which $p(t)$ signals persistent activity, is around $\nu_c = 0.90(5)$ for $\lambda = 1$, the most efficient activity propagating branching process. However, it is difficult to locate the critical point exactly because the evolution slows down and exhibits oscillating as well as logarithmic corrections. The decay at the critical point is slower than the mean-field decay, characterized by $\delta = 0.5$. It may even be ultra-slow (i.e. logarithmic) as in disordered directed percolation in $d < 4$ dimensions [42].

Below the transition point, the avalanche survival exponent changes continuously in the range $0.2 < \delta < 0.7$ as shown in the inset of Fig. 3. These effective exponents exhibit stabilization of $\delta_{\text{eff}}(t)$ for $10^2 < t < 10^5$. Using the scaling relation (9), we get dynamical scaling exponents in the GP region: $1.2 < \tau_t \leq 1.7$, overlapping with the human brain experimental values $1.5 < \tau < 2.4$ of [27].

At and below the critical point, the avalanche size distributions also exhibit non-universal power-law tails, as shown in Fig. 4, characterized by $\tau > 1.25(2)$, overlapping with the experiments $1 < \tau < 1.6$ of [27]. The collapse of averaged avalanche distributions $\Pi(t)$ for fixed temporal sizes T as in [11] was also studied. The inset of Fig. 4 displays a good a collapse, obtained for avalanches of temporal sizes $T = 25, 63, 218, 404$, using a vertical scaling $\Pi(t)/T^{0.34}$, which is near the experimental findings reported in [11]. Note also the asymmetric shape which is in agreement with the experiments but could not be reproduced by the model of Ref. [11].

In Ref. [83], the connectome modifications included random removal of up to 20% of directed connections and flipping the signs of the weights W_{ij} of randomly selected edges. The random link removal affects the long-range connections more, as they are less frequent, than the short-range ones. Thus, this modification makes the connectome closer to reality in the sense of statistics, as it introduces asymmetry in the connections in an expected fraction and compensates the distortion of the MRI diffusion tensor imaging

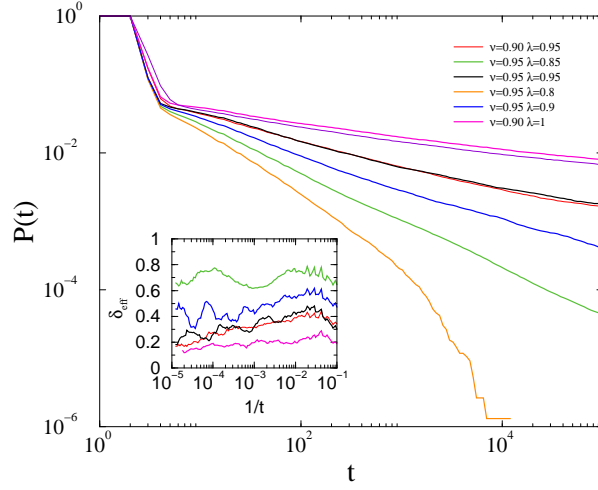


Figure 3. Avalanche survival probability of the two-state threshold model using $K = 0.25$, $\nu = 0.90, 0.95$ and $\lambda = 0.8, 0.85, 0.90, 0.95, 1$ (as shown by the legends). Inset: Local slopes of the same curves in opposite order showing saturation of the non-universal exponents in the GP. Figure from [94].

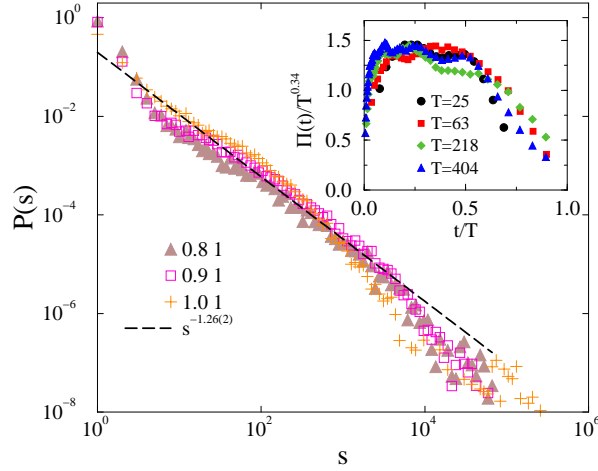


Figure 4. Avalanche size distribution of the two-state threshold model at $K = 0.25$, $\nu = 1$ and $\lambda = 1, 0.9, 0.8$. Dashed line: power-law fit to the $\lambda = 0.8$ case. Inset: Avalanche shape collapse for $T = 25, 63, 218, 404$ at $\lambda = 0.86$ and $\nu = 0.95$. Figure from [83].

method, which underestimates local fiber tracts [99]. However, this edge thinning made the dynamics slower and the exponents a little bit smaller than the experimental values, suggesting that additional factors should also be taken into account.

In Ref. [94], the two-state model study was extended to a three-state, refractory threshold version as well as to a time-dependent threshold version with a binary distribution $\{K, K - \Delta K\}$. Numerical evidence was provided for the robustness of the GP for both modifications. However, the GP shrank if the amplitude of time dependence was stronger because, for large ΔK , the system could jump over the control-parameter

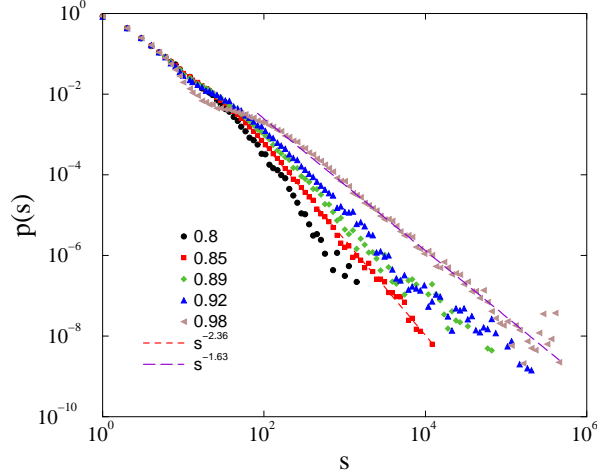


Figure 5. Avalanche size distributions in the sub-critical phase of the three-state threshold model with 5% inhibitory links at $K = 0.2$, $\nu = 1$ and $\lambda = 0.8, 0.85, 0.89, 0.92, 0.94, 0.98$ (bottom to top curves). Dashed lines show power-law fits for the tails of the $\lambda = 0.85$ and the $\lambda = 0.98$ curves with $\tau = 1.63(1)$ and $\tau = 2.36(2)$ respectively.

region where the GP occurs.

This robustness was studied with and without the presence of negative-weighted edges. Figure 5 shows refractory model results for the avalanche sizes in case of 5% randomly flipped inhibitory links at $K = 0.2$. Non-universal scaling is evident in the GP sub-critically for $0.8 < \nu \leq 0.98$, characterized by exponent values $1.63 \leq \tau \leq 2.63$. These values are close to the characteristic times of human experiments [27]: $1 < \tau < 1.6$. The model results do not change much if inhibitory links are absent [94].

Figure 6 shows some results for the time-dependent two-state model, where the threshold $K = 0.1$ was lowered to $K = 0.09$ at randomly selected time steps with probability 0.5. In this case, the GP shrank approximately to the region $0.483 < \lambda < 0.513$. Thus, the critical point moved down to $\lambda \simeq 0.51(1)$ with respect to the time independent model. Therefore, the avalanche size exponent in the GP varies as $1.36(1) < \tau < 1.58(1)$, well inside the experimental range $1 < \tau < 1.6$ of [27].

4. Critical synchronization dynamics on the Connectome

One of the most fundamental models showing phase synchronization is the Kuramoto model of interacting oscillators [51]. It was originally defined on full graphs, corresponding to mean-field behaviour [100]. The critical dynamical behaviour has recently been explored on random graphs [101,102]. A phase transition in the Kuramoto model can happen only above the lower critical dimension $d_l = 4$ [103]. In lower dimensions, a true, singular phase transition in the $N \rightarrow \infty$ limit is not possible, but partial synchronization can emerge with a smooth crossover if oscillators are strongly coupled.

The Kuramoto model describes interacting oscillators with phases $\theta_i(t)$ located at

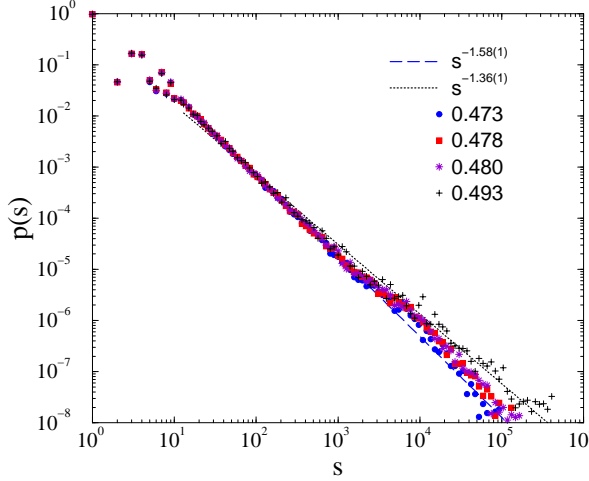


Figure 6. Avalanche size distributions of the two-state threshold model with 30% inhibitory links using time varying threshold: $K = 0.1$, $\Delta K = 0.01$, at $\nu = 0.95$ and $\lambda = 0.473, 0.478, 0.480, 0.483, 0.493$, (bottom to top curves). Dashed lines show power-law fits $s^{-1.58(1)}$ and $s^{-1.36(1)}$ for the tails of the $\lambda = 0.493$ and $\lambda = 0.473$ curves. Figure from [94].

N nodes of a network, which evolve according to the dynamical equation

$$\dot{\theta}_i(t) = \omega_{i,0} + K \sum_j W_{ij} \sin[\theta_j(t) - \theta_i(t)] + s \xi(i). \quad (14)$$

Here, summation is performed over neighbouring nodes of i . $\omega_{i,0}$ is the intrinsic frequency of the i -th oscillator, drawn from a $g(\omega_{i,0})$ distribution. For distributions with flat top the transition becomes discontinuous [104, 105]. Usually, a Gaussian distribution with zero mean and unit variance is used to study a continuous synchronization transition. Oscillatory behaviour is possible in the presence of quenched $g(\omega_{i,0})$ self-frequencies. In their absence, Eq. (14) describes a nonequilibrium XY model (e.g. see [95]). We can also add an annealed noise $\xi(i)$ process, to emulate thermal fluctuations, which is a Gaussian white noise in general, coupled by the amplitude s [105].

The global coupling K is the control parameter of this model by which we can tune the system between asynchronous and synchronous states. One usually follows the synchronization transition through studying the Kuramoto order parameter defined by

$$R(t) = \frac{1}{N} \left| \sum_{j=1}^N e^{i\theta_j(t)} \right|, \quad (15)$$

which is non-zero above a critical coupling strength $K > K_c$ or tends to zero for $K < K_c$ as $R \propto \sqrt{1/N}$. At K_c , R exhibits growth as

$$R(t, N) = N^{-1/2} t^\eta f_\uparrow(t/N^{\tilde{z}}), \quad (16)$$

with the dynamical exponents \tilde{z} and η , if the initial state is incoherent. Otherwise, the initial state decays as

$$R(t, N) = t^{-\delta} f_\downarrow(t/N^{\tilde{z}}), \quad (17)$$

characterized by the dynamical exponent δ . Here f_\uparrow and f_\downarrow denote different scaling functions.

The (noiseless) Kuramoto equation exhibits Galilean symmetry [52, 106]. It is invariant to the global shift of a mean rotation frame $\bar{\omega} \rightarrow \bar{\omega}'$ and the oscillation-size dependence can also be gauged out by the following transformation: $\omega_i \rightarrow a\omega'_i$, $t \rightarrow (1/a)t'$ and $K \rightarrow aK'$. Therefore, for small values of a , corresponding to empirical data, we can obtain the same results as for $\sigma = 1$ at rescaled, late times and using small global couplings. This scale invariance is an important technical benefit, which can be exploited to simulate ultra-slow oscillations at time scales < 0.01 Hz, shown by human-brain fMRI measurements [107, 108].

To locate the transition from de-synchronized to synchronized states, one can increase the global coupling K and determine $R(t)$ by averaging over thousands of realizations with different, independent initial conditions. The computer experiments are done by applying random initialization of phases with uniform distribution $\theta_i(0) \in (0, 2\pi]$. Using parallelized Runge-Kutta-4 algorithm for NVIDIA graphic cards (GPU) a $\times 40$ increase in the throughput could be achieved with respect to a single 12-core CPU. Figure 7 shows an example for the growth of the Kuramoto order parameter on the *KKI-18* connectome. The transition is smooth, but the transition point can be

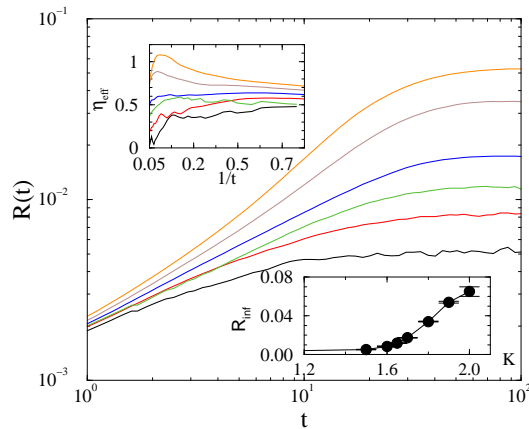


Figure 7. Growth of the average R on the *KKI-18* graph near the synchronization transition point for $K = 1.5, 1.6, 1.65, 1.7, 1.8, 1.9$ (bottom to top curves). Upper left inset: Effective exponents, defined as (13) for the same data, down inset: steady state $R(t \rightarrow \infty)$ as the function of the global coupling. Figure from [84]

estimated visually via the inflexion condition, which separates up (convex) and down (concave) bending curves for times $t < 20$ before finite size causes saturation of $R(t)$. Looking at the local slopes, we can estimate this crossover at $K_c = 1.60(5)$, with an effective scaling exponent $\eta_{\text{eff}} \simeq 0.6(1)$. This is smaller than the $\eta = 0.75$ mean-field value of the Kuramoto model [101]. The lower inset in Fig. 7 shows that the steady state values $R(t \rightarrow \infty, K)$ exhibit a low level of synchronization even above the transition point.

To describe synchronization avalanches in terms of the Kuramoto order parameter,

we can consider processes starting from fully de-synchronized initial states by a single phase perturbation (or by an external phase shift at a node), followed by growth and return to $R(t_x) = 1/\sqrt{N}$, corresponding to the disordered state of N oscillators. In the simulations one can measure the first return, crossing times t_x in many random realizations of the system. In [84, 105], the return time was estimated by $t_x = (t_k + t_{k-1})/2$, where t_k was the first measured crossing time when R fell below $1/\sqrt{N} = 0.001094$ (see Fig. 8).

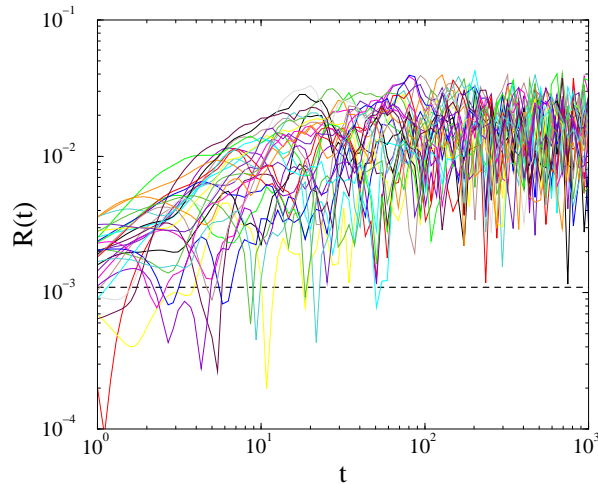


Figure 8. Evolution of $R(t)$ for many single realizations on the *KKI-18* graph at $K = 1.7$. The dashed line shows the threshold value $R = 1/\sqrt{N} = 0.001094$, used for the characteristic time measurements. Figure from [84].

Following a histogramming procedure, one can obtain distributions of $p(t_x)$, which exhibit power-law tails for $1.2 < K \leq 1.7$, characterized by the exponents $1 < \tau_t < 2$ (see Fig. 9), which are in the range of the in vivo human neuro-experiments: $1.5 < \tau_t < 2.4$ of [27]. At $K = 1.6$ (i.e. near the transition point), we find $\tau_t = 1.2(1)$. Above the transition point, the decay $p(t_x) \sim 1/t$ marks a synchronized phase, where return to de-synchronization can take long. The exponent value $\tau_t = 1.2(1)$ at the transition suggests that the real brain works in the sub-critical phase, where we can still observe dynamical criticality. The phase with the non-universal power laws is reminiscent of GPs, but modules create frustrated synchronization regions [53, 55, 56] with meta-stability and chimera-like states [54]. For comparison, on a large two-dimensional lattice with additional random, long-range links, the mean-field value $\tau_t \simeq 1.6(1)$ was obtained [102].

The addition of weak noise does not change these results as can be seen for $s = 1$ at $K = 1.4$ in Figure 9. However, stronger noise causes deviations, which are difficult to investigate as numerical precision of the applied Runge-Kutta-4 integration breaks down in case of large differences that are generated by strong fluctuations and produced by annealed noise.

Additionally, when the signs of the weights on a randomly selected 5% of links

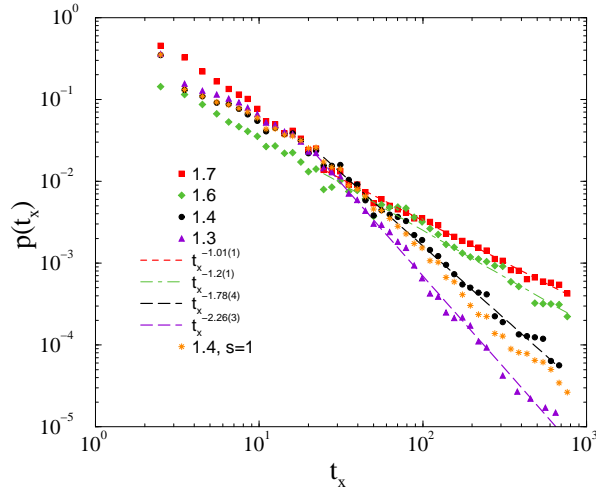


Figure 9. Duration distribution of t_x on the *KKI-18* model for growth $K = 1.7$ (boxes), 1.6 (diamonds), 1.4 (bullets), 1.3 (up triangles), 1.4 with $s = 1$ noise (asterisks). The dashed lines shows power-law fits for the tail region $t_x > 20$. Figure from [105]

are flipped as $W''_{ij} = -W'_{ij}$, dynamical scaling was found to be invariant. Such links suppress local synchronization and can thus be considered as an inhibition mechanism. The crossover to synchronization occurs at $K_c = 1.9(1)$, slightly higher than for the original *KKI-18* network. The tails of the $p(t_x)$ probability distributions exhibit power laws with $1 < \tau_t \leq 2$ in the $1.4 < K < 1.8$ region.

In [83], the robustness of the GP with threshold-model dynamical behaviour was tested by randomly neglecting 20% of links in one direction. In [84], the neglect of all links in one direction ($W''_{ij} = -W'_{ij}$, $W''_{ji} = 0$) was investigated. Even in this extremely an-isotropic situation, an extended scaling region emerges below the smooth transition point.

Finally, graphs with 5%, 10% and 20% inhibitory nodes were created by flipping the signs of (outward or inward) link weights of these randomly selected sites. Below the synchronization transition point, which is at $K_c = 1.7(1)$ for 5%, we can find again a frustrated synchronization region, where power-law-tailed de-synchronization durations occur as before (see Fig. 10). The exponent values are in the range $1 < \tau_t < 2$.

5. Conclusions and Outlook

Neural variability makes the brain more efficient [109], and one must, therefore, consider its effect in modelling. To study this effect, extended dynamical simulations have been performed on large human connectome models. Weight heterogeneity of such structural graphs is too strong to allow critical behaviour to appear. Thus, weight normalized versions were considered, which model local homeostasis by synaptic inhibition mechanisms.

After comparing available human brain connectomes using network topology

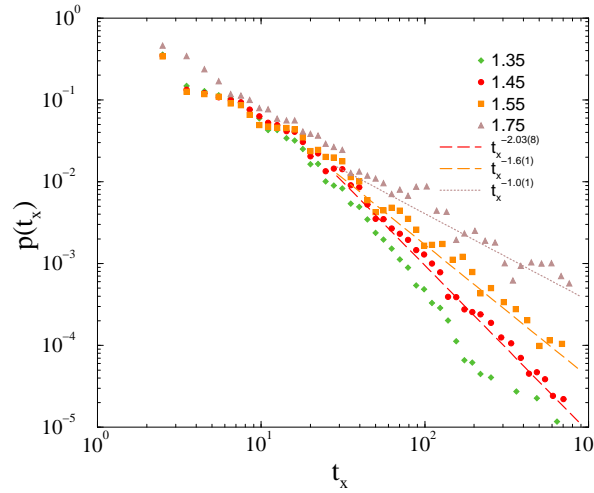


Figure 10. Duration distribution of t_x on the *KKI-18* model if 5% of the nodes are inhibitory and $K = 1.35$ (diamonds), $K = 1.45$ (bullets), 1.55 (boxes), 1.75 (triangles). The dashed line shows power-law fits to the tail region: $t_x > 20$. Figure from [84]

analysis, one network, called *KKI-18*, was selected as a representative. For the threshold model, critical exponents in the range $1.4 < \tau_t < 1.7$ and $1.5 < \tau < 2$, close to neural experimental values [16], were found.

Regarding the oscillatory Kuramoto model, we conclude that quenched disorder in the self-frequencies causes power-law tails in the dynamical behaviour of chimera-like states at the edge of criticality. These non-universal power laws resemble Griffiths Phase effects. The scaling laws also resemble results for the second-order Kuramoto model on power grids below the synchronization transition [110]. We found characteristic dynamical time exponents $1 < \tau_t < 2$, overlapping with LRTC experiments. A recent analysis [111] on new and publicly available data from both anesthetized and freely moving animals also concluded that, if the cortex demands both extreme modes of operation (synchronized and de-synchronized) for different functions, it may be advantageous to self-organize near and hover over the critical point between the two modes. Our large scale simulation results show that the characteristic time exponents can be reproduced with this assumption sub-critically.

It is important to note, that while some rough tuning of the control parameters might be necessary to get closer to the critical point, one can see dynamical criticality even *below a phase transition point* without external activation, which is a safe expectation for brain systems [23]. Recent experiments suggest slightly sub-critical brain states *in vivo*, devoid of dangerous over-activity linked to epilepsy.

The dynamical scaling behaviour has been found to be robust, supporting universality. Although the Kuramoto model could be considered too simplistic to describe the brain; in the weak-coupling limit equivalence of phase-oscillator and integrate-and-fire models was found [112], which may hold for the sub-critical region, where dynamical scaling was observed. This provides support for the edge-of-criticality

hypothesis for oscillating systems near and below the synchronization transition point. Additive weak annealed noise, added to the Kuramoto equation also resulted in invariance of the scaling [105]. Gaussian noises with amplitudes not larger than those of the quenched Gaussian self-frequencies do not affect the previous results within numerical precision. This means that time-dependent, thermal-like noise does not destroy or alter the dynamical scaling behaviour of this model. We also pointed out that the empirical results with ultra-slow oscillations can be transformed onto zero-mean Gaussian frequencies as the consequence of the Galilean symmetry of the Kuramoto equation [105]. Positiveness of the $g(\omega_i)$ distribution is necessary in the brain, as we do not expect neural oscillators to 'rotate backwards'. This corresponds to the question of asymmetric distribution of natural frequencies, such that for $g(\omega_i) = 0$ for $\omega_i < 0$. It has been shown that in case of uni-modal $g(\omega_i)$ -s only the first derivative, the flatness of $g(\omega_i)$, matters. Without a flat top, like an asymmetric triangle, one obtains the same universal critical behaviour ($\beta = 1/2$) as for the original Kuramoto model with zero-centered symmetric Gaussian [113]. Thus we expect the same dynamical behaviour for an asymmetric, truncated Gaussian with $g(\omega_i) = 0$ for $\omega_i < 0$.

An interesting continuation could be the study of the effect of phase shifts, caused by finite signal propagation in the neural network or the introduction of a threshold, as in integrate-and-fire models, although by universality of critical systems we do not expect qualitative changes in the scaling behaviour.

Although these connectomes do not provide a true network of the brain, as for example the nodes themselves are built from thousands of neurons and may not map the gray matter links well, the can still lead to the best meso-level approximation for critical brain dynamics. Further research is under way to extend our approaches to large, exact, but still not full connectomes available at present.

Sub-sampling ambiguities may also cause differences from the experiments. Our mesoscopic model could also open up the possibility to clarify this with the possibility of changing the scale of averaging of simulation results.

Meta-stability and hysteresis are also common in brain behaviour. They are related to the ability to sustain stimulus-selective persistent activity for working memory [114]. The brain rapidly switches from one state to another in response to stimulus, and it may remain in the same state for a long time after the end of the stimulus. Meta-stability and hysteresis occur in general at first-order phase transitions. However, at hybrid type or mixed order transitions dynamical criticality can coexist with them. Using synthetic hierarchical modular networks, it has recently been shown that even GPs can be found below the discontinuous transition using threshold type models, where the excitation level are high enough to cause fragmentation of the possible activity patterns [115]. In brain science language this means different topology for the structural and the functional networks. This allows GPs in high dimensional, small-world graphs, which for simpler systems was hypothesized to be impossible, leaving out only mean-field like behaviour [116]. An interesting direction would be to extend such model analysis using real connectome graphs.

Finally, the mechanistic studies reviewed here offer a causal account of the role of synchronization and specifically of heterogeneity for criticality at the whole-brain level. This mechanistic framework is extremely promising and relevant not only to deepen our understanding of healthy brain functions but also for its breakdown in neuropsychiatric diseases. Our whole-brain model perspective might help to improve the diagnosis, and design of therapies after understanding the subtle synchronization effects relevant in mental diseases.

Acknowledgments

G.Ó is supported by the National Research, Development and Innovation Office NKFIH under Grant No. K128989 and the Project HPC-EUROPA3 (INFRAIA-2016-1-730897) from the EC Research Innovation Action under the H2020 Programme.

G.D. is supported by a Spanish national research project (ref. PID2019-105772GB-I00 MCIU AEI) funded by the Spanish Ministry of Science, Innovation and Universities (MCIU), State Research Agency (AEI); HBP SGA3 Human Brain Project Specific Grant Agreement 3 (grant agreement no. 945539), funded by the EU H2020 FET Flagship programme; SGR Research Support Group support (ref. 2017 SGR 1545), funded by the Catalan Agency for Management of University and Research Grants (AGAUR); Neurotwin Digital twins for model-driven non-invasive electrical brain stimulation (grant agreement ID: 101017716) funded by the EU H2020 FET Proactive programme; euSNN European School of Network Neuroscience (grant agreement ID: 860563) funded by the EU H2020 MSCA-ITN Innovative Training Networks; CECH The Emerging Human Brain Cluster (Id. 001-P-001682) within the framework of the European Research Development Fund Operational Program of Catalonia 2014-2020; Brain-Connects: Brain Connectivity during Stroke Recovery and Rehabilitation (id. 201725.33) funded by the Fundacio La Marato TV3; Corticity, FLAG-ERA JTC 2017, (ref. PCI2018-092891) funded by the Spanish Ministry of Science, Innovation and Universities (MCIU), State Research Agency (AEI).

J. K. is supported by the Helmholtz Initiative and Networking Funds via the W2/W3 programme, project number W2/W3-026.

We gratefully acknowledge computational resources provided by the Hungarian National Supercomputer Network, the BSC Barcelona and the HZDR computing center.

References

- [1] Attwell D and Laughlin S B 2001 *Journal of Cerebral Blood Flow & Metabolism* **21** 1133–1145 pMID: 11598490
- [2] Raichle M E 2006 *Science* **314** 1249–1250
- [3] Fiser J, Berkes P, Orban G and Lengyel M 2010 *Trends in Cognitive Sciences* **14** 119–130
- [4] Tavor I, Jones O P, Mars R B, Smith S M, Behrens T E and Jbabdi S 2016 *Science* **352** 216–220
- [5] Cole M S, Ito T, Bassett D S and H S D 2016 *Nature Neuroscience* **19** 1718—1726
- [6] Osher D E, Brissenden J A and Somers D C 2019 *Journal of Neurophysiology* **122** 232–240 pMID: 31066602

- [7] Deco G and Jirsa V K 2012 *Journal of Neuroscience* **32** 3366–3375
- [8] Deco G, Ponce-Alvarez A, Hagmann P, Romani G, Mantini D and Corbetta M 2014 *Journal of Neuroscience* **34** 7886–7898
- [9] Senden M, Reuter N, van den Heuvel M P, Goebel R and Deco G 2017 *NeuroImage* **146** 561–574
- [10] Shew W L and Plenz D 2013 *The Neuroscientist* **19** 88–100 pMID: 22627091
- [11] Friedman N, Ito S, Brinkman B A W, Shimono M, DeVille R E L, Dahmen K A, Beggs J M and Butler T C 2012 *Phys. Rev. Lett.* **108**(20) 208102
- [12] Kinouchi O and Copelli M 2006 *Nature Physics* **2** 348–352
- [13] Chialvo D R 2010 *Nature Physics* **6** 744–750
- [14] Larremore D B, Shew W L and Restrepo J G 2011 *Phys. Rev. Lett.* **106**(5) 058101
- [15] Muñoz M A 2018 *Rev. Mod. Phys.* **90**(3) 031001
- [16] Beggs J and Plenz D 2003 *J. Neuroscience* **23** 11167
- [17] Mazzoni A, Broccard F D, Garcia-Perez E, Bonifazi P, Ruaro M E and Torre V 2007 *PLOS ONE* **2** 1–12
- [18] Pasquale V, Massobrio P, Bologna L, Chiappalone M and Martinoia S 2008 *Neuroscience* **153** 1354–1369
- [19] Hahn G, Petermann T, Havenith M N, Yu S, Singer W, Plenz D and Nikolić D 2010 *Journal of Neurophysiology* **104** 3312–3322 pMID: 20631221
- [20] Shriki O, Alstott J, Carver F, Holroyd T, Henson R N, Smith M L, Coppola R, Bullmore E and Plenz D 2013 *Journal of Neuroscience* **33** 7079–7090
- [21] Tagliazucchi E, Balenzuela P, Fraiman D and Chialvo D 2012 *Frontiers in Physiology* **3** 15
- [22] Scott G, Fagerholm E D, Mutoh H, Leech R, Sharp D J, Shew W L and Knöpfel T 2014 *Journal of Neuroscience* **34** 16611–16620
- [23] Priesemann V, Wibral M, Valderrama M, Pröpper R, Le Van Quyen M, Geisel T, Triesch J, Nikolić D and Munk M H J 2014 *Frontiers in Systems Neuroscience* **8** 108
- [24] Bellay T, Klaus A, Seshadri S and Plenz D 2015 *Elife* **4** e07224
- [25] Hahn G, Ponce-Alvarez A, Monier C, Benvenuti G, Kumar A, Chavane F, Deco G and Frégnac Y 2017 *PLOS Computational Biology* **13** 1–29
- [26] Seshadri S, Klaus A, Winkowski D and et al 2018 *Transl Psychiatry* **8**
- [27] Palva J, Zhigalov A, Hirvonen J, Korhonen O, Linkenkaer-Hansen K and Palva S 2013 *Proceedings of the National Academy of Sciences of the United States of America* **110** 3585–3590
- [28] Ódor G 2008 *Universality in nonequilibrium lattice systems: Theoretical foundations*
- [29] Yaghoubi M, De Graaf T, Orlandi J, Giroto F, Colicos M and Davidsen J 2018 *Scientific Reports* **8**
- [30] Fosque L J, Williams-García R V, Beggs J M and Ortiz G 2021 *Phys. Rev. Lett.* **126**(9) 098101
- [31] Stumpf M P H, Wiuf C and May R M 2005 *Proceedings of the National Academy of Sciences* **102** 4221–4224
- [32] Levina A and Priesemann V 2017 *Nature Communications* **8**
- [33] Beggs J M and Plenz D 2003 *Journal of Neuroscience* **23** 11167–11177
- [34] Priesemann V, Wibral M, Valderrama M, Pröpper R, Le Van Quyen M, Geisel T, Triesch J, Nikolić D and Munk M H J 2014 *Frontiers in Systems Neuroscience* **8** 108
- [35] Hagmann P, Cammoun L, Gigandet X, Meuli R, Honey C J, Wedeen V J and Sporns O 2008 *PLOS Biology* **6** e159
- [36] Honey C J, Sporns O, Cammoun L, Gigandet X, Thiran J P, Meuli R and Hagmann P 2009 *Proceedings of the National Academy of Sciences* **106** 2035–2040
- [37] Moretti P and Muñoz M A 2013 *Nature Communications* **4** 2521
- [38] Gastner M T and Ódor G 2016 *Scientific Reports* **6** 27249
- [39] Stassinopoulos D and Bak P 1995 *Physical Review E* **51** 5033–5039
- [40] Pruessner G 2012 *Self-organised criticality: Theory, models and characterisation*
- [41] Ódor G, Dickman R and Ódor G 2015 *Scientific Reports* **5** 14451
- [42] Vojta T 2006 *Journal of Physics A: Mathematical and General* **39** R143–R205

- [43] Griffiths R B 1969 *Phys. Rev. Lett.* **23** 17–19
- [44] Ódor G 2004 *Phys. Rev. E* **89** 042102
- [45] Karsai M, Jo H H and Kaski K 2018 *SpringerBriefs in Complexity*
- [46] Cota W, Ferreira S C and Ódor G 2016 *Phys. Rev. E* **93** 032322
- [47] Johnson S, Torres J J and Marro J 2013 *PLoS ONE* **8** e50276
- [48] Penn Y, Segal M and Moses E 2016 *Proceedings of the National Academy of Sciences of the United States of America* **113** 3341–3346
- [49] Di Santo S, Villegas P, Burioni R and Muñoz M 2018 *Proceedings of the National Academy of Sciences of the United States of America* **115** E1356–E1365
- [50] Freyer F, Roberts J A, Becker R, Robinson P A, Ritter P and Breakspear M 2011 *Journal of Neuroscience* **31** 6353–6361
- [51] Kuramoto Y 2012 *Chemical Oscillations, Waves, and Turbulence* Springer Series in Synergetics (Springer Berlin Heidelberg) ISBN 9783642696893
- [52] Acebrón J, Bonilla L, Vicente C, Ritort F and Spigler R 2005 *Reviews of Modern Physics* **77** 137–185
- [53] Villegas P, Moretti P and Muñoz M 2014 *Scientific Reports* **4**
- [54] Abrams D M and Strogatz S H 2004 *Phys. Rev. Lett.* **93**(17) 174102
- [55] Villegas P, Hidalgo J, Moretti P and Muñoz M 2016 Complex synchronization patterns in the human connectome network pp 69–80
- [56] Millán A, Torres J and Bianconi G 2018 *Scientific Reports* **8**
- [57] Feng Y E and Li H H 2015 *Chinese Physics Letters* **32** 060502
- [58] Pikovsky A and Rosenblum M 2008 *Phys. Rev. Lett.* **101**(26) 264103
- [59] Laing C R 2009 *Physica D: Nonlinear Phenomena* **238** 1569 – 1588
- [60] Zhu Y, Zheng Z and Yang J 2014 *Phys. Rev. E* **89**(2) 022914
- [61] Cabral J, Hugues E, Sporns O and Deco G 2011 *NeuroImage* **57** 130 – 139
- [62] Sporns O, Tonomi G and Kötter R 2005 *PLOS Computational Biology* **1** e42
- [63] Landman B A, Huang A J, Gifford A, Vikram D S, Lim I A L, Farrell J A D, Bogovic J A, Hua J, Chen M, Jarso S, Smith S A, Joel S, Mori S, Pekar J J, Barker P B, Prince J L and van Zijl P C M 2011 *NeuroImage* **54** 2854–2866
- [64] Delettre C, Messé A, Dell L A, Fouquet O, Heuer K, Larrat B, Meriaux S, Mangin J F, Reillo I, de Juan Romero C, Borrell V, Toro R and Hilgetag C C 2019 *Network Neuroscience* **3** 1038–1050
- [65] Eguíluz V M, Chialvo D R, Cecchi G A, Baliki M and Apkarian A V 2005 *Physical Review Letters* **94** 018102
- [66] van den Heuvel M P, Stam C J, Boersma M and Hulshoff Pol H E 2008 *NeuroImage* **43** 528–539
- [67] Kaiser M 2011 *NeuroImage* **57** 892–907
- [68] Pasquale V, Massobrio P, Bologna L L, Chiappalone M and Martinoia S 2008 *Neuroscience* **153** 1354–1369
- [69] Expert P, Lambiotte R, Chialvo D R, Christensen K, Jensen H J, Sharp D J and Turkheimer F 2011 *Journal of The Royal Society Interface* **8** 472–479
- [70] Humphries M, Gurney K and Prescott T 2006 *Proceedings of the Royal Society B: Biological Sciences* **273** 503–511
- [71] Ivković M, Kuceyeski A and Raj A 2012 *PLOS ONE* **7** e35029
- [72] Allard A and Serrano M Á 2020 *PLOS Computational Biology* **16** e1007584
- [73] Teimouri M and Gupta A K 2013 *Journal of Data Science* **11** 403–414
- [74] Burnham K P and Anderson D R 2002 *Model Selection and Multimodel Inference: A Practical Information-Theoretic Approach* 2nd ed (New York: Springer-Verlag) ISBN 978-0-387-95364-9
- [75] Watts D J and Strogatz S H 1998 *Nature* **393** 440–442
- [76] Vaessen M J, Hofman P A M, Tijssen H N, Aldenkamp A P, Jansen J F A and Backes W H 2010 *NeuroImage* **51** 1106–1116
- [77] Hilgetag C C and Goulas A 2016 *Brain Structure and Function* **221** 2361–2366
- [78] Humphries M D and Gurney K 2008 *PLOS ONE* **3** e0002051

- [79] Moretti P and Muñoz M A 2013 *Nature Communications* **4** 2521
- [80] 2015 Neurodata, <https://neurodata.io>
- [81] Gray Roncal W, Koterba Z H, Mhembere D, Kleissas D M, Vogelstein J T, Burns R, Bowles A R, Donavos D K, Ryman S, Jung R E, Wu L, Calhoun V and Vogelstein R J 2013 Migraine: Mri graph reliability analysis and inference for connectomics *2013 IEEE Global Conference on Signal and Information Processing* pp 313–316
- [82] Traag V A, Waltman L and van Eck N J 2019 *Scientific Reports* **9** 5233
- [83] Ódor G 2016 *Phys. Rev. E* **94** 062411
- [84] Ódor G and Kelling J 2019 *Scientific Reports* **9** 19621
- [85] Remme M and Wadman W 2012 *PLoS Computational Biology* **8**
- [86] Drost F, Do A L and Gross T 2013 *Journal of the Royal Society Interface* **10**
- [87] Hellyer P, Jachs B, Clopath C and Leech R 2016 *NeuroImage* **124** 85–95
- [88] Hellyer P, Clopath C, Kehagia A, Turkheimer F and Leech R 2017 *PLoS computational biology* **13** e1005721
- [89] Kaiser M and Hilgetag C 2010 *Frontiers in Neuroinformatics* **4**
- [90] Azouz R and Gray C 2000 *Proceedings of the National Academy of Sciences of the United States of America* **97** 8110–8115
- [91] Hütt M T, Jain M, Hilgetag C and Lesne A 2012 *Chaos, Solitons and Fractals* **45** 611–618
- [92] Rocha R, Koççillari L, Suweis S, Corbetta M and Maritan A 2018 *Scientific Reports* **8**
- [93] Haimovici A, Tagliazucchi E, Balenzuela P and Chialvo D R 2013 *Phys. Rev. Lett.* **110**(17) 178101
- [94] Ódor G 2019 *Physical Review E* **99** 012113
- [95] Ódor G 2004 *Rev. Mod. Phys.* **76**(3) 663–724
- [96] Kandel E R 2013 *Principles of neural science* 5th ed (The McGraw-Hill Companies)
- [97] Grassberger P and de la Torre A 1979 *Ann. Phys.* **122** 373
- [98] Muñoz M A, Dickman R, Vespignani A and Zapperi S 1999 *Phys. Rev. E* **59** 6175
- [99] Jbabdi S and Johansen-Berg H 2015 *Brain Connectivity* **1** 169
- [100] Hong H, Chaté H, Park H and Tang L H 2007 *Physical Review Letters* **99**
- [101] Choi C, Ha M and Kahng B 2013 *Physical Review E - Statistical, Nonlinear, and Soft Matter Physics* **88**
- [102] Juhász R, Kelling J and Ódor G 2019 *Journal of Statistical Mechanics: Theory and Experiment* **2019** 053403
- [103] Hong H, Park H and Choi M 2005 *Physical Review E - Statistical, Nonlinear, and Soft Matter Physics* **72**
- [104] Pazó D 2005 *Phys. Rev. E* **72**(4) 046211
- [105] Ódor G, Kelling J and Deco G 2021 *J. Neurocomputing* ? ? (Preprint [arXiv:1912.06018](https://arxiv.org/abs/1912.06018))
- [106] Pikovsky A, Kurths J, Rosenblum M and Kurths J 2003 *Synchronization: A Universal Concept in Nonlinear Sciences* Cambridge Nonlinear Science Series (Cambridge University Press) ISBN 9780521533522
- [107] Ponce-Alvarez A, Deco, Hagmann P, Romani G, Mantini and Corbetta D 2015 *PLoSComput Biol* **11**
- [108] Deco G, Kringsbach M, Jirsa V and Ritter P 2017 *Scientific Reports* **7**
- [109] Orbán G, J F and Lengyel M 2016 *Neuron* 530—543
- [110] Ódor G and Hartmann B 2018 *Physical Review E* **98**
- [111] Fontenele A J, de Vasconcelos N A P, Feliciano T, Aguiar L A A, Soares-Cunha C, Coimbra B, Dalla Porta L, Ribeiro S, Rodrigues A J a, Sousa N, Carelli P V and Copelli M 2019 *Phys. Rev. Lett.* **122**(20) 208101
- [112] Politi A and Rosenblum M 2015 *Physical Review E - Statistical, Nonlinear, and Soft Matter Physics* **91**
- [113] Basnarkov L and Urumov V 2008 *Phys. Rev. E* **78**(1) 011113
- [114] Durstewitz D, Seamans J K and Sejnowski T J 2000 *Nat. Neurosci.* **3** 1184
- [115] Ódor G and de Simoni B 2021 *Phys. Rev. Research* **3**(1) 013106

[116] Muñoz M A, Juhász R, Castellano C and Ódor G 2010 *Phys. Rev. Lett.* **105** 128701